

Explanations of MTF discrepancy in grating-based X-ray differential phase contrast CT imaging

Yuhang Tan,¹ Jiecheng Yang,¹ Hairong Zheng,^{1,2} Dong Liang,^{1,2} Peiping Zhu,³ and Yongshuai Ge^{1,2, a)}

¹⁾*Research Center for Medical Artificial Intelligence, Shenzhen Institute of Advanced Technology, Chinese Academy of Sciences, Shenzhen, 518055, China*

²⁾*Paul C Lauterbur Research Center for Biomedical Imaging, Shenzhen Institute of Advanced Technology, Chinese Academy of Sciences, Shenzhen 518055, China*

³⁾*Institute of High Energy Physics, Chinese Academy of Sciences, Beijing 100049, China*

As a multi-contrast X-ray computed tomography (CT) imaging system, the grating-based Talbot-Lau interferometer is able to generate the absorption contrast and differential phase contrast (DPC) images concurrently. However, experiments found that the absorption CT (ACT) images have better spatial resolution, i.e., higher modulation transfer function (MTF), than the differential phase contrast CT (DPCT) images. Until now, the root cause of such observed discrepancy has not been rigorously investigated. Through physical experiments, this study revealed that the phase grating in the Talbot-Lau interferometer induces direct superposition of paired split absorption signals and inverse superposition of paired split phase signals via diffraction. Further simulation experiments demonstrated that this splitting leads to a reduction in MTF in both ACT and DPCT images, with distinct superposition mechanisms contributing to the lower MTF in DPCT. Besides, such MTF discrepancy may also be affected in a minor extent by object composition, sample size, beam spectra and detector pixel size. Based on this study, the spatial resolution could be optimized when designing a grating-based DPC imaging system.

^{a)}Authors to whom correspondence should be addressed: Yongshuai Ge (ys.ge@siat.ac.cn).

I. INTRODUCTION

By coupling a grating-based Talbot-Lau interferometer, the conventional X-ray computed tomography (CT) imaging system can simultaneously assess multiple contrasts^{1,2}, such as the absorption contrast, the differential phase contrast (DPC), and the dark-field contrast. For materials composed of light elements, the sensitivity of X-ray phase imaging may be three orders of magnitude greater than that of absorption imaging. Therefore, the phase information is particularly important in low-density object imaging, and has been considered promising during biomedical imaging.

As in many other imaging systems, the modulation transfer function (MTF) plays a crucial role in quantitatively evaluating the spatial resolution limit of a grating-based DPC imaging system. Interestingly, it was experimentally observed that DPCT shows much lower MTF than ACT³. Despite of the plausible explanations, unfortunately, the root causes of such MTF discrepancy in grating-based X-ray DPCT imaging systems have not been rigorously investigated.

Relatedly, as the Talbot-Lau system resolution increases to nanoscale by copuling a zone plate, DPCT images have been confirmed to transition into the superposition of paired split phase signals⁴. Considering the zone plate merely serves an amplifying role, the splitting phenomenon is also present in Talbot-Lau system without the zone plate. The natural question arises: does this splitting phenomenon occur in ACT images, and is it the root cause of the MTF discrepancy between ACT and DPCT.

To interpret, this study starts from the X-ray diffraction theory for the π -phase grating interferometer system incorporates with object. Theoretical derivations indicate that the detected absorption and DPC signals are both composed by a pair of diffracted signals split by a particular distance denoted as Δs , which is related to the X-ray wavelength, grating period, and the distance from the grating to detector. Specifically, the formations of the detected absorption and DPC signals are opposite: the former is generated by the direct-superposition of the paired split absorption signals, and the latter is generated by the inverse-superposition of the paired split phase signals. Because of such distinct signal superposition mechanism, we assume that different levels of edge blurring may occur on the finally reconstructed ACT and DPCT images. In other words, MTF discrepancy would appear in a grating-based X-ray imaging system. To verify, physical experiments and nu-

merical simulation studies are performed. Additionally, object composition, sample size, beam spectra and detector pixel size are also investigated to qualify their potential impacts on such MTF discrepancy.

II. THEORY

In this work, the scalar wave fields of an assumed Talbot grating interferometer are calculated using the Fresnel diffraction theorem under the paraxial approximation⁵. In brief, the Fresnel diffraction field $U_{\text{out}}(x')$ after propagation by a distance d is denoted as:

$$U_{\text{out}}(x') = \int U_{\text{in}}(x) \frac{e^{ik(d + \frac{(x'-x)^2}{2d})}}{\sqrt{i\lambda d}} dx. \quad (2.1)$$

where $U_{\text{in}}(x)$ is the input, λ and $k(= \frac{2\pi}{\lambda})$ represent the wavelength and wave number of X-ray, respectively.

The scalar wave field right before the object plane, which is located d_1 distance downstream of a quasi-monochromatic point source $\delta(x_0 - \eta)$, is equal to:

$$U_1(x_1) = \frac{e^{ik(d_1 + \frac{(x_1 - \eta)^2}{2d_1})}}{\sqrt{i\lambda d_1}}, \quad (2.2)$$

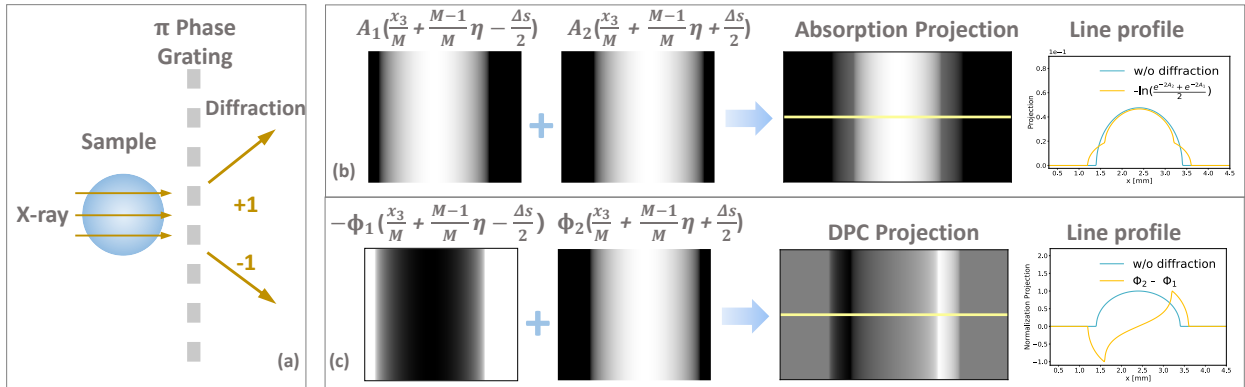


FIG. 1. (a) X-ray beam is diffracted after the π phase grating in Talbot interferometer. The -1 and +1 diffraction orders carry different sample information that are split by a distance of $\Delta s = \frac{2\lambda d_3}{p_1}$. (b) In absorption imaging, superposition is performed on the paired positive signals. (c) In DPC imaging, superposition is performed on the paired negative and positive signals. It is clear that the absorption and DPC projections own different edge blurring effects and thus may result in MTF discrepancy.

where η is the off-axis distance of the point source. Next, such wave field $U_1(x_1)$ is modulated into $U_1(x_1) \cdot e^{-k\alpha(x_1) - ik\phi(x_1)}$ after penetrating through a thin object with a complex refractive index $n = 1 - \delta + i\beta$. Herein, the absorption signal $\alpha(x_1) = \int \beta(x_1) dz$ and the phase signal $\phi(x_1) = \int \delta(x_1) dz$.

Immediately, the wave field on the surface of phase grating (G1) is derived as:

$$U_2(x_2) = \frac{e^{ik(d_1+d_2+\frac{(x_2-\eta)^2}{2(d_1+d_2)}-\Psi(\frac{d_2\eta+d_1x_2}{d_1+d_2}))}}{\sqrt{i\lambda(d_1+d_2)}}, \quad (2.3)$$

where $\Psi(x) = \phi(x) - i\alpha(x)$. The wave field $U_2'(x_2)$ after G1 can be expressed as follows:

$$U_2'(x_2) = U_2(x_2) T(x_2) = U_2(x_2) \sum_{n=-\infty}^{\infty} a_n e^{\frac{2in\pi x_2}{p_1}}, \quad (2.4)$$

where $T(x_2)$ denotes the periodic transmission function of G1, p_1 denotes the grating period and a_n denotes the complex Fourier coefficient. Finally, the wave field $U_3(x_3)$ on the detection plane (d_3 distance away from G1) is expressed as:

$$\begin{aligned} U_3(x_3) &= \sum_{n=-\infty}^{\infty} a_n \frac{e^{ik(d_1+d_2+d_3+S(x_3))}}{\sqrt{i\lambda(d_1+d_2+d_3)}}, \\ S(x_3) &= \frac{n\lambda(d_1x_3+d_2x_3+d_3\eta)}{(d_1+d_2+d_3)p_1} - \frac{2n^2\pi^2d_3(d_1+d_2)}{(d_1+d_2+d_3)k^2p_1^2} \\ &+ \frac{(x_3-\eta)^2}{2(d_1+d_2+d_3)} - \Psi\left(\frac{\eta kp_1(d_2+d_3)+d_1(kp_1x_3-2n\pi d_3)}{(d_1+d_2+d_3)kp_1}\right). \end{aligned} \quad (2.5)$$

Herein, we assume G1 is a π phase grating with 0.5 duty cycle. If only considering the most dominant diffraction orders (± 1), then the detected beam intensity approximately equals:

$$\begin{aligned} I(x_3) &= |U_3(x_3, n)|^2 \approx \frac{8A_3^2}{\pi^2} \left(\frac{1}{2}(e^{-2A_1} + e^{-2A_2}) \right. \\ &\quad \left. + e^{-(A_1+A_2)} \cos(Cx_3 + \Theta - \Phi_1 + \Phi_2) \right), \end{aligned} \quad (2.6)$$

and

$$\begin{aligned}
C &= \frac{4\pi(d_1 + d_2)}{(d_1 + d_2 + d_3)p_1}, \\
\Theta &= \frac{4\pi d_3 \eta}{(d_1 + d_2 + d_3)p_1}, \\
M &= \frac{d_1 + d_2 + d_3}{d_1}, \\
A_1 &= k\alpha \left(\frac{x_3}{M} - \frac{\lambda d_3}{Mp_1} + \frac{M-1}{M} \eta \right), \\
A_2 &= k\alpha \left(\frac{x_3}{M} + \frac{\lambda d_3}{Mp_1} + \frac{M-1}{M} \eta \right), \\
\Phi_1 &= k\phi \left(\frac{x_3}{M} - \frac{\lambda d_3}{Mp_1} + \frac{M-1}{M} \eta \right), \\
\Phi_2 &= k\phi \left(\frac{x_3}{M} + \frac{\lambda d_3}{Mp_1} + \frac{M-1}{M} \eta \right), \\
A_3 &= \frac{e^{ik(d_1+d_2+d_3+\frac{(x_3-\eta)^2}{2(d_1+d_2+d_3)})}}{\sqrt{i\lambda(d_1+d_2+d_3)}},
\end{aligned} \tag{2.7}$$

where M denotes the geometric magnification, and $2\pi/C$ corresponds to the fringe period. Note that the absorption grating G2, which is usually added to generate large periodic Moiré fringes, is ignored in this theoretical derivation. Eventually, the extracted absorption contrast signal (A) and DPC signal ($\Delta\Phi$) of the sample are:

$$\begin{aligned}
e^{-2A(x_3)} &= 0.5 \times (e^{-2A_1} + e^{-2A_2}), \\
\Delta\Phi(x_3) &= \Phi_2 - \Phi_1.
\end{aligned} \tag{2.8}$$

Obviously, Eq. (2.8) demonstrates that the acquired absorption and DPC signals are formed via two completely different mechanisms: the former is resulted from the direct-superposition of the paired split absorption signals, and the latter is resulted from the inverse-superposition of the paired split phase signals. Intuitively, such different signal recombination mechanisms on the projections may cause different edge blurring effects and thus lead to MTF discrepancy in the reconstructed CT images, see the illustration in Fig. 1 for more details.

III. PHYSICAL EXPERIMENT AND RESULTS

The physical experiments based on inverse Talbot-Lau interferometer are designed to validate the theory in Eq. (2.8). Specifically, the distance d_0 between source and G_0 is 50.0

mm , the distance d_1 between G_0 and G_1 is 177.5 mm , the distance d_2 between G_1 and sample is 100 mm , and the distance d_3 between sample and G_2 is 1701.4 mm . The source grating G_0 has a period of $2.4\text{ }\mu m$, the phase grating G_1 has a period of $4.37\text{ }\mu m$, and the absorption grating G_2 has a period of $2.18\text{ }\mu m$. The mean X-ray beam energy is 28 keV , and the detector pixel size is $4.6\mu m \times 4.6\mu m$. The sample is a gold line with a diameter of $25\text{ }\mu m$. Under these conditions, the theoretically splitting distance Δs is $36.5\text{ }\mu m$, enabling the detection of the splitting phenomenon.

To verify, the experiments employ different grating combinations: $G_s = G_0 + G_1 + G_2$, $G_0 + G_1$, G_0 , and noG_s , and the phase and absorption images are shown in Fig. 2(a). In addition, the vertically average profiles are compared. Specifically, the sample width of $\Delta A(G_s)$ obtained by fitting to reduce noise is the same as $\Delta\phi(G_s)$, as shown in Fig. 2(b). The sample width in the absorption image with G_1 (e.g. $A(G_s), A(G_0 + G_1)$) are larger than that without G_1 (e.g. $A(G_0), A(noG_s)$), as shown in Fig. 2(c). When $A(G_0)$ or $A(noG_s)$ is substituted into Eq. (2.8) with $\Delta s = 46\mu m$, its sample width becomes consistent with $A(G_0 + G_1)$ or $A(G_s)$, aligning with the theoretical expectation with an error of about two pixels, as shown in Fig. 2(d). These physical experiment results verified that the splitting phenomenon also exists in the ACT image. However, due to factors such as excessive system length and low X-ray energy, each projection takes nearly a day to acquire, making it impossible to obtain experimental MTF results. Therefore, simulations are employed to explore the root cause of the MTF discrepancy between ACT and DPCT.

IV. SIMULATION EXPERIMENTS AND RESULTS

The numerical simulation platform was developed in Python (Version: 3.9). The propagation of wave fields was implemented via the fast Fourier transform (FFT). More details of this numerical simulation platform can be found in⁶.

The first simulation employs the same system configuration as used in³. By doing so, the viability of the theoretical assumption can be validated. The ACT and DPCT images with $10\mu m \times 10\mu m$ pixel size were reconstructed from the filtered-back-projection (FBP) algorithms⁷, see Fig. 3(a) and (b). In particular, the Ramp filter was used for ACT reconstruction, and the Hilbert filter was used for DPCT reconstruction⁸. Results are plotted in Fig. 3(c). As seen, the simulated and measured MTF curves of ACT and DPCT exhibit

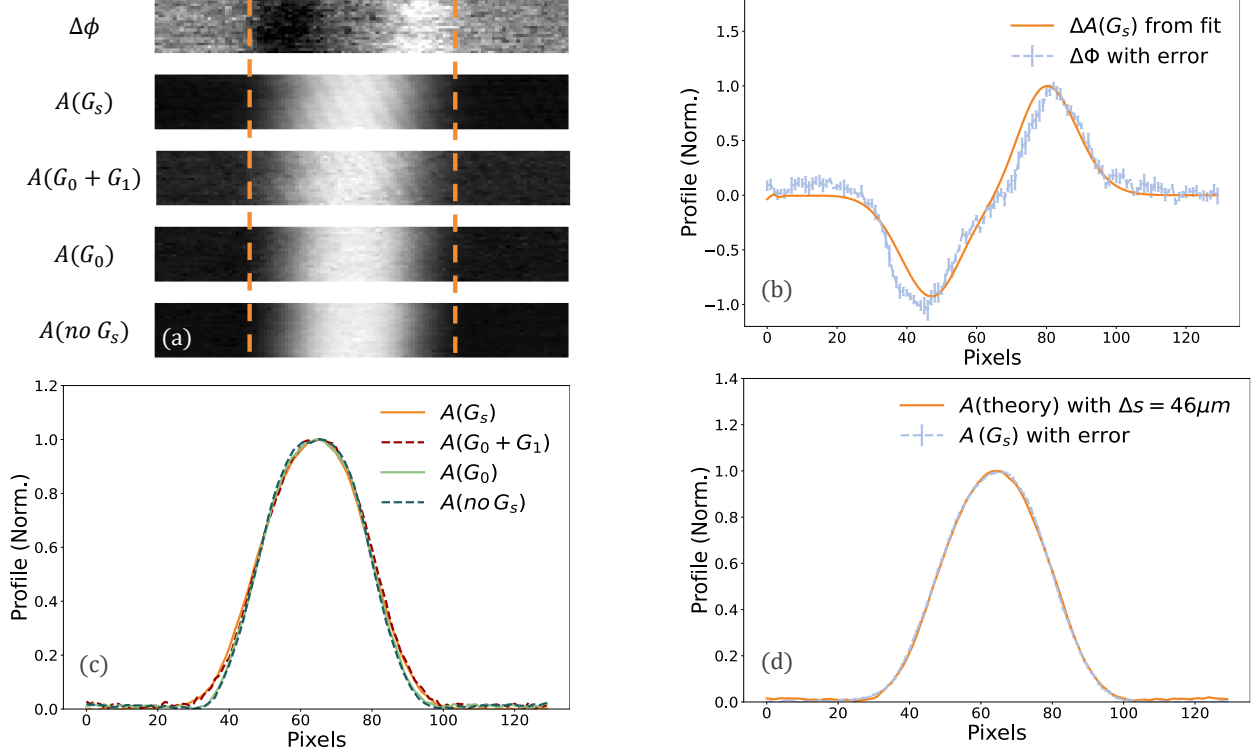


FIG. 2. (a) The phase and absorption images of the gold line sample with different grating combinations. Comparison of vertically averaged profiles: (b) $\Delta A(G_s)$ and $\Delta\phi$; (c) Different grating combinations; (d) $A(G_s)$ and $A(\text{theory})$ with $\Delta s = 46\mu m$.

high agreements. This demonstrates the feasibility of our provided explanation: the inverse-superposition in phase imaging degrades the image spatial resolution more significantly than the direct-superposition in absorption imaging, provided that the standard ACT and DPCT image reconstruction algorithms are implemented.

Additional simulations were performed to investigate the dependency on Δs , object composition, beam spectra, sample size (D) and detector pixel size (Δdel), correspondingly. Results are shown in Fig. 3. Plots in Fig. 3(d) are numerically calculated from Eq. (2.8) for different Δs . Undoubtedly, results demonstrate that the different formation mechanisms of absorption signal and DPC signal are the primary cause of MTF discrepancy. The simulated results are plotted in Fig. 3(e). It is found that the MTFs of both ACT and DPCT get lower as Δs increases. This is understandable since the edge blurring effect gets more severe. It is worth mentioning that the adjustment of Δs is achieved by varying the period of G_1 , and $\Delta s < \Delta del$ is assumed.

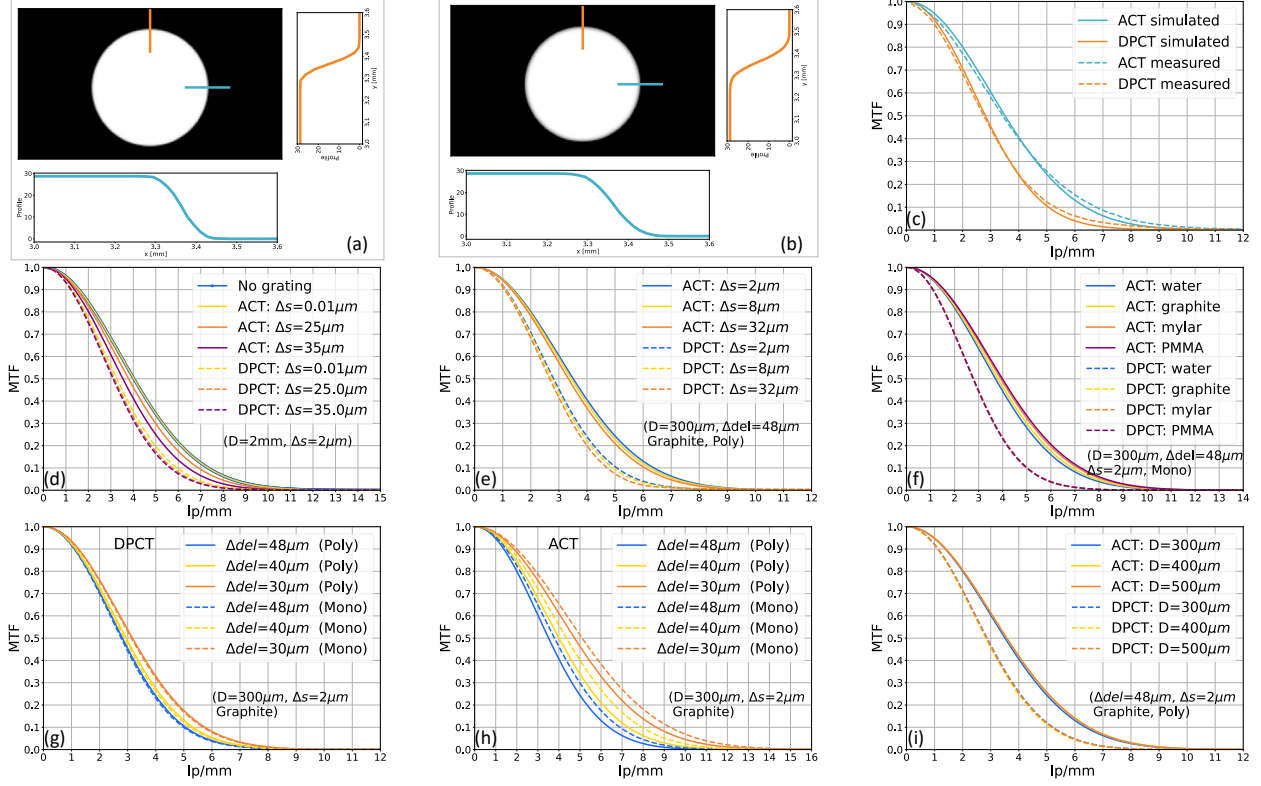


FIG. 3. (a) and (b) depict the reconstructed ACT and DPCT images of the graphite, respectively. Edge profiles along both horizontal and vertical directions are plotted. (c) Comparison results of measured MTFs and simulated MTFs of ACT and DPCT. (d) Theoretically estimated MTF curves for different Δs according to Eq. (2.8). (e) Numerically simulated MTF responses for different Δs . (f) Dependence of MTF curves on object compositions. (g) MTFs of DPCT for different detector pixel size Δdel and beam spectra. (h) MTFs of ACT for different Δdel and beam spectra. (i) MTF responses for different object size D . Note that other imaging parameters are listed inside each plot.

As listed in Table. I, four different materials are simulated. Results are depicted in Fig. 3(f). Interestingly, the MTFs of ACT get higher as the ratio δ/β increases, whereas, the MTFs of DPCT are approximately the same for different object compositions.

The energy dependent results of the MTFs are plotted in Fig. 3(g) and Fig. 3(h) along with varied detector pixel sizes. As seen, the MTF increases as the pixel size reduces. For DPCT, the impact of beam spectra is negligible. As a contrary, the ACT shows slightly better MTF performance with monochromatic 25 keV X-ray beams. The polychromatic X-ray beam is simulated under 40 kVp with 1.0 mm Al filtration. It is noticed that the

TABLE I. Results of MTF for different materials.

	water	graphite	mylar	PMMA
$\delta(\times 10^{-7})$	3.69	3.90	4.84	4.26
$\beta(\times 10^{-11})$	10.48	9.39	9.14	7.45
δ/β	3521	4153	5295	5718
MTF _{10%} ^{ACT} [lp/mm]	6.7	6.9	7.1	7.2
MTF _{10%} ^{DPCT} [lp/mm]	5.0	5.0	5.0	5.0

sample size has little impact on the MTF of DPCT, see the results in Fig. 3(i). The MTF of ACT becomes slightly better as the object size increases.

V. DISCUSSIONS AND CONCLUSION

This paper provides a feasible explanation for the MTF discrepancy of ACT and DPCT acquired from the same grating-based interferometer system, and the different superposition of the projection signals might be the main cause. Physical experiment results show that the detected absorption projection follows the direct-superposition of the paired split absorption signals, and the detected DPC projection follows the inverse-superposition of the paired split phase signals. Numerical simulation results show that the inverse-superposition is more easy to degrade the edge sharpness. Therefore, the MTF of DPCT is lower than that of ACT. Numerical simulations demonstrate the high agreement with the previous experimental measurements. Besides, the diffraction induced splitting distance Δs , object composition, beam spectra, sample size and detector pixel size are further investigated. Results find that the MTFs of both ACT and DPCT would get lower as Δs increases. However, the ACT always outperforms the DPCT. Additionally, the object composition, sample size, beam spectra and detector pixel size may also affect the MTF.

Based on this study, we think additional attention is required when discussing the spatial resolution in different X-ray interferometer systems and imaging tasks, particularly for ACT and DPCT. Note that the current simulations are implemented for small signal splitting Δs , i.e., within one detector pixel. For systems having larger Δs (or small detector pixel dimension), however, innovative signal extraction techniques^{4,9} need to be considered. Essentially, more rigorous ACT and DPCT image reconstruction algorithms are desired to generate high

precision ACT and DPCT images for any X-ray interferometer system. To do so, we think the derived projection signal models in Eq. (2.8) would be helpful in initiating such future studies. Finally, the MTF discrepancy effect would be evaluated for the 0.5π -phase grating interferometer system¹ and other none grating-based DPC imaging approaches such as the diffraction enhanced imaging¹⁰.

In conclusion, a feasible explanation for the MTF discrepancy phenomenon of ACT and DPCT in grating-based X-ray interferometer system is investigated in this study. Upon it, the performance of the spatial resolution of a given multi-contrast grating-based imaging system can be optimized.

VI. FUNDING

This project is supported by the National Natural Science Foundation of China (12027812), Guangdong Basic and Applied Basic Research Foundation (2021A1515111031), and the Youth Innovation Promotion Association of the Chinese Academy of Sciences (2021362).

VII. DISCLOSURES

The authors declare no conflicts of interest.

VIII. DATA AVAILABILITY

Data underlying the results presented in this paper are not publicly available at this time but may be obtained from the authors upon reasonable request.

REFERENCES

- ¹A. Momose, “Recent advances in x-ray phase imaging,” [Japanese Journal of Applied Physics](#) **44**, 6355–6367 (2005).
- ²T. Weitkamp, A. Diaz, C. David, F. Pfeiffer, M. Stampanoni, P. Cloetens, and E. Ziegler, “X-ray phase imaging with a grating interferometer,” [Opt. Express](#) **13**, 6296–6304 (2005).

- ³K. Li, J. Zambelli, N. Bevins, Y. Ge, and G.-H. Chen, “Spatial resolution characterization of differential phase contrast CT systems via modulation transfer function (MTF) measurements,” *Physics in Medicine and Biology* **58**, 4119–4135 (2013).
- ⁴W. Yashiro, Y. Takeda, A. Takeuchi, Y. Suzuki, and A. Momose, “Hard-x-ray phase-difference microscopy using a fresnel zone plate and a transmission grating,” *Phys. Rev. Lett.* **103**, 180801 (2009).
- ⁵Y. Ge, J. Chen, P. Zhu, J. Yang, S. Deng, W. Shi, K. Zhang, J. Guo, H. Zhang, H. Zheng, and D. Liang, “Dual phase grating based x-ray differential phase contrast imaging with source grating: theory and validation,” *Opt. Express* **28**, 9786–9801 (2020).
- ⁶J. Yang, P. Zhu, D. Liang, H. Zheng, and Y. Ge, “X-ray phase-sensitive microscope imaging with a grating interferometer: Theory and simulation,” *Chinese Physics B* **31**, 098702 (2022).
- ⁷Z. Qi and G.-H. Chen, “Direct fan-beam reconstruction algorithm via filtered backprojection for differential phase-contrast computed tomography,” *X-Ray Optics and Instrumentation* **2008** (2008), 10.1155/2008/835172.
- ⁸H. Zhifeng, K. Kejun, L. Zheng, Z. Peiping, Y. Qingxi, H. Wanxia, W. Junyue, and Z. Di, “Direct computed tomographic reconstruction for directional-derivative projections of computed tomography of diffraction enhanced imaging,” *Applied Physics Letters* **89** (2006), 10.1063/1.2219405.
- ⁹H. Takano, Y. Wu, J. Irwin, S. Maderych, M. Leibowitz, A. Tkachuk, A. Kumar, B. Hornberger, and A. Momose, “Comparison of image properties in full-field phase x-ray microscopes based on grating interferometry and zernike’s phase contrast optics,” *Applied Physics Letters* **113** (2018).
- ¹⁰V. N. Ingal and E. A. Beliaevskaya, “X-ray plane-wave topography observation of the phase contrast from a non-crystalline object,” *Journal of Physics D: Applied Physics* **28**, 2314 (1995).